

# HANDHELD FISHEYE MULTICAMERA SYSTEM: SURVEYING MEANDERING ARCHITECTONIC SPACES IN OPEN-LOOP MODE – ACCURACY ASSESSMENT

L. Perfetti<sup>1</sup>, F. Fassi<sup>1</sup>

<sup>1</sup> Politecnico di Milano, Dept. of Architecture, Built environment and Construction engineering (ABC), Italy  
(luca.perfetti, francesco.fassi)@polimi.it

## Commission II

**KEY WORDS:** Multicamera, Fisheye, Photogrammetry, Mobile mapping, Architecture, Cultural Heritage

### ABSTRACT:

The task of digitalizing meandering complex spaces in 3D is a challenging one even with the most advanced instrumentation like light-weight terrestrial laser scanner or portable/wearable Mobile Mapping Systems (MMSs). The complexity and extension of architectonic spaces such as staircases, corridors and passages are such that the acquisition time using static devices becomes prohibitive and the accuracy using mobile devices gets affected by drift error leading to warped models or requiring abundant control measurements. This paper presents a photogrammetric portable fisheye multicamera solution for the 3D survey of complex areas that aims at being both handy and fast in the acquisition as well as more reliable and accurate than common MMSs. The paper showcases a stress test conducted on five complex reconstruction trajectories selected from the meandering connection passages of Milan's Cathedral. The tests are constructed as worst-case scenario to evaluate the accuracy and drift error amount of the proposed system in open-ended unconstrained paths. The results, though still suffering from moderate drift error, highlights the potential of the solution, especially in retaining the overall shape and orthogonality of the architectonic elements acquired.

## 1. INTRODUCTION

The process of three-dimensional digitization of the built environment, especially of the valuable cultural heritage architectures, is today of imperative importance, required by management, administration, and technical offices. This process is essential so that many other activities can follow, such as: maintenance, management, conservation, and cultural valorisation of these assets. To this end, there are now many established practices and continuous innovation aimed at surveying the built environment in 3D. The different techniques and instruments used, such as terrestrial photogrammetry, terrestrial laser scanners and portable laser scanners, offer as final output of the survey a 3D point cloud able to describe the geometry of the surveyed spaces by itself or, able to serve as a basis for the subsequent phase of restitution or modelling. Regardless, therefore, of the tools used in the survey phase, the final output is comparable between the different approaches and therefore the choice to use one or another instrumentation depends primarily on technical evaluations regarding the feasibility of operations: speed, cost, practicality, and the accuracy and resolution required to the final data.

One of the main critical elements in the digitization of architectural heritage is the problem of mapping those areas characterized by poor accessibility: such as tunnels, corridors, stairwells, service spaces, and narrow spaces in general, for which the instrumental options to choose from are reduced.

Measuring instruments designed to be handy, portable, and fast in data acquisition are increasingly present on the market today. Among these, in the category of terrestrial laser scanners there is the Leica RTC360; while in the category of portable scanners we find handheld solutions such as Geoslam ZEB REVO, Kaarta Stencil and Contour; backpack solutions such as Leica Pegasus Backpack and Gexcel Heron; and even drone solutions for indoor use, such as those produced by Emesent. However, all these solutions do not yet satisfy all scenarios required for the digitization of built heritage. Among the main limitations are: (i) the poor accuracy of mobile mapping systems when they have to be used in long acquisitions in open-loop mode; (ii) the minimum scanning range of the sensors used by both terrestrial and portable

scanners when they have to be used in confined spaces; and (iii) the complexity of instrument handling and consequent lengthening of acquisition times in the field with regard to even the most manageable terrestrial scanners when they have to be used in complex confined spaces.

On the other hand, there are no commercial solutions on the market that exploit a photogrammetric approach, which has great potential to overcome the current limitations of the state of the art.

This paper presents a new measuring instrument (Figure 1, patent pending No. 102021000000812): a fisheye multicamera device that can be used on the move and operated handheld by a single operator, designed and prototyped for the rapid three-dimensional survey of complex and narrow architectural spaces. The purpose of this instrument is to obtain a complete and accurate survey, in the form of a point cloud, in a short time that can facilitate the acquisition of complex narrow spaces and thus promote complete three-dimensional digitization in all its parts even of the most complex architecture.

The objective of this paper is to evaluate the accuracy and reliability of this multicamera system through field tests, in particular the robustness of the system with respect to error propagation in long acquisitions in open-loop mode.

### 1.1 Related Works

Multi-camera photogrammetric systems designed for mobile mapping are widespread in the literature where these are chosen mainly for three reasons: (i) the speed of acquisition in the field, (ii) the cost-effectiveness of the solution in comparison with the state of the art, (iii) the possibility of automatically scaling the three-dimensional reconstruction based on the known dimensional relationships between the rigid cameras composing the system. Among the authors that proposed a multicamera system for the acquisition of extensive narrow spaces there are: Koehl et al., (2016), who evaluated different stereo configurations of four GoPro action cameras mounted on a rigid bar for the fast 3D reconstruction of urban tunnels; Meyer et al. (2020), that presented a system composed of multiple off-the-shelf mirrorless cameras to achieve the fast 3D reconstruction of tunnels and human-equivalent inspection; Panella et al., (2020),

that presented an evaluation comparison test between a multi-camera array of GoPro cameras and a terrestrial laser scanner. Other authors presented successful application of stereo multi-cameras to be employed underwater (Shortis et al., 2007; Nocerino et al., 2018; Nocerino et al., 2019) exploiting the advantages in scaling the results without the need of additional measurements. While others presented and tested multi-camera panoramic configurations: Teo (2015) used a multi-GoPro panoramic rig to survey indoor environments and staircases, Barazzetti et al. (2017) presented some results using the commercial Samsung Gear360 pano-camera, while Barazzetti et al. (2020) proposed a novel approach to integrate 360° imagery in restoration projects. Our approach involves a rig in which the cameras are arranged in a stereoscopic configuration and exploits the use of fisheye lenses and their wide angle of view to survey narrow spaces (Perfetti et al., 2017).

## 2. MULTICAMERA SYSTEM

The proposed multi-camera system (Figure 1) is a portable device that consists of a hand-held probe containing the mapping unit and a small backpack housing the power supply and a computer. The mapping unit consists of five industrial grade cameras (Flir BFS 50S5) employing a 2/3" colour sensor with a resolution of 2448 x 2048 pixels and a detector pitch of 3.45µm and of LED lamps that points to the front and to the sides of the device for indoor use. The cameras are coupled with fisheye lenses that span a field of view of 190° allowing overall imaging of the entire surroundings of the instrument except for the operator. From the probe, the operator can control the automatic acquisition of a series of images while autonomously navigating the environment to be measured.

The cameras in the system are arranged according to Perfetti (2020) aimed at being most effective when used in narrow tunnel (around 1m wide) with significant separation between one another (distance between side front cameras and side back cameras are ~220mm).

Of fundamental importance for the system is the stability of the rig geometry during the movement, this is ensured by the synchronization of the camera captures and by the use of global shutter sensors.

An adequate synchronisation of the cameras ensures that the location of the cameras at the moment of image capture reflects the geometry of the multicamera at rest even while moving, thus avoiding delays between acquisitions to distort the relative location of the images. The synchronisation of the system has been tested for accuracy as in Perfetti (2020) and resulted in a max synch error of ~200µs which fits the intended use case scenario of the device that is intended to be used at walking speed.



Figure 1. Picture of the prototype of the multicamera system.

The use of global shutter sensors is also important for the cameras to be used in motion avoiding the distortion introduced by the rolling shutter effect so that accurate multicamera constraints can be exploited during processing.

The main advantage of the proposed multicamera is its manoeuvrability combined with the ease of use that allows to acquire in a single sequence complex environments and different areas such as outdoor environments, indoor environments and detailed elements like niches. Moreover, provided that the cameras' shooting speed is set correctly, the acquisition does not suffer from the shaking or vibrations caused by uncertain terrain or complex or chaotic acquisitions.

## 3. ACCURACY ASSESSMENT

With the aim to evaluate the performance of the proposed multicamera system, it was decided to test it in challenging tasks and to simulate worst case scenarios. A case study was identified that had the necessary characteristics in terms of complexity and accessibility of spaces to test the proposed approach highlighting its limitations. The chosen case study consists of five narrow paths that are part of the service passages of the Milan Cathedral. These paths (Figure 2 and Figure 3) were chosen according to their length and complexity. These paths wind along the spaces of the cathedral, intercepting environments with different characteristics such as: spiral staircases, internal passages, small rooms, external areas, illuminated environments and completely dark environments. Aside for "Path A", the paths are open-ended: the acquisition with the multicamera starts at one end of the path and end on the opposite end. A return acquisition is also usually performed, but the return acquisition follows the same trajectory of the outward acquisition. The whole winding of the paths is left unconstrained and check points (CPs) are used to measure the drift error.

For all tests the accuracy of the reconstruction was assessed with two checks: (i) a "global check", where all points available are used as CPs; and (ii) a "max drift check", where only the beginning of one end of the open loop is constrained and the drift error is measured on all other CPs.

For the "max drift check" the constraint points are used as ground control points (GCPs) in a seven parameters similarity transformation and the opposite end is used as check. This is done with the intention of simulating the worst-case scenario of an open-ended extensive path, for which no GCPs are available, to experimentally estimate the drift error of the proposed system.

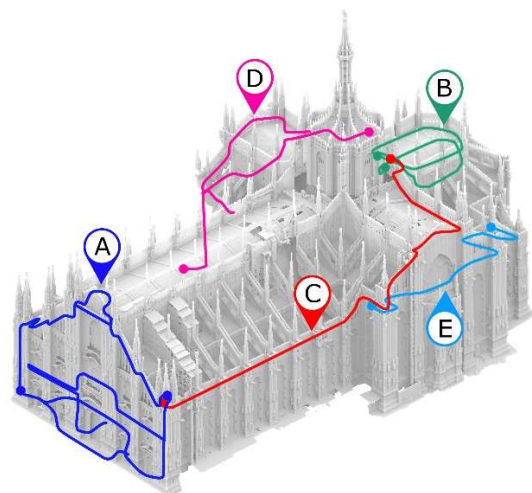


Figure 2. test paths acquired with the multi-camera on an orthographic view of the Milan's Cathedral.



Figure 3. On field acquisitions inside a narrow spiral staircase.

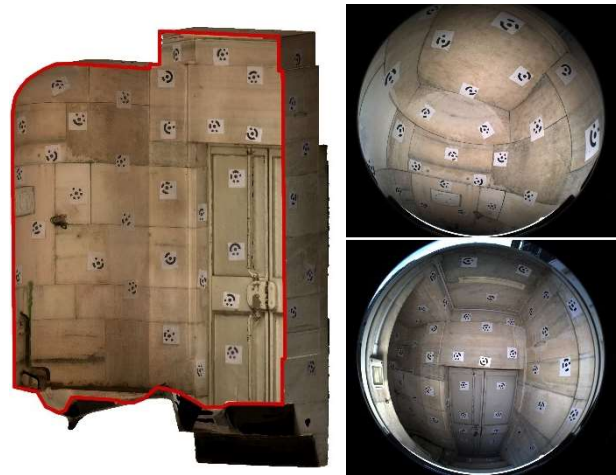


Figure 4. Section view of the calibration testfield used (left), and two images acquired by the multi-camera system (right).

### 3.1 The test paths

**3.1.1 Path A:** this path is the only closed loop dataset; it covers all passages hidden in the Milan Cathedral façade including 3 narrow spiral staircases ~70cm wide (Figure 6). The acquisition took 70min to complete for a length of 290m.

**3.1.2 Path B:** this path starts on the rooftop of the apse and connects to a series of rooms at the extrados of the apse vaults (Figure 7). The acquisition was 295m long and took 35 min.

**3.1.3 Path C:** this passageway connects the high level of the cathedral roofs with the lower level and continues until it reaches the façade (Figures 7). This acquisition was performed in the forward direction only for a length of 245m completed in 15 min.

**3.1.4 Path D:** this passage focuses on the north transept, connecting the church level with the rooftop level via a long spiral staircase (Figures 8). The whole acquisition took 120 min and covered a length of 465m.

**3.1.5 Path E:** this passage is concentrated at the low level of the north transept roofs (Figures 9), is 256m long and took 45 min to be acquired.

## 4. CALIBRATION

The multicamera system was carefully calibrated to take advantage of the rig rigid configuration in improving the reconstruction accuracy. This was done by calculating the internal orientation parameters of the individual cameras and the relative orientation parameters between them:

**4.1.1 Internal orientation parameters:** they were calculated using a strongly textured test-field of known coordinates (Perfetti et. al., 2018; Perfetti, 2020). The calculated parameters were then used as initial values in the following data processing performed using Agisoft Metashape.

**4.1.2 Multicamera relative constraint:** regarding the relative orientations, only the baselines between the cameras were calculated and not the relative rotations. These were then used as constraints in the processing in Metashape.

		1-2	1-3	1-4	1-5	2-3	2-4	2-5	3-4	3-5	4-5
C1	median	258.44	101.18	94.42	254.86	290.29	221.82	203.17	173.99	214.04	285.35
	MAD	0.17	0.15	0.11	0.11	0.16	0.10	0.24	0.13	0.08	0.18
	median (FD)	258.41	101.15	94.42	254.83	290.27	221.80	203.14	173.98	214.03	285.32
C2	median	258.45	101.19	94.43	254.86	290.31	221.83	203.17	174.00	214.03	285.34
	MAD	0.16	0.15	0.11	0.13	0.17	0.11	0.24	0.11	0.08	0.19
	median (FD)	258.41	101.17	94.43	254.83	290.28	221.81	203.16	173.98	214.02	285.30

Table 1. Estimated baselines obtained from calibration 1 before the acquisition (C1) and calibration 2 after the acquisition (C2). The table reports the median and MAD of the whole dataset and the median of the filtered dataset (FD) after outlier removal. All values are expressed in millimetres.

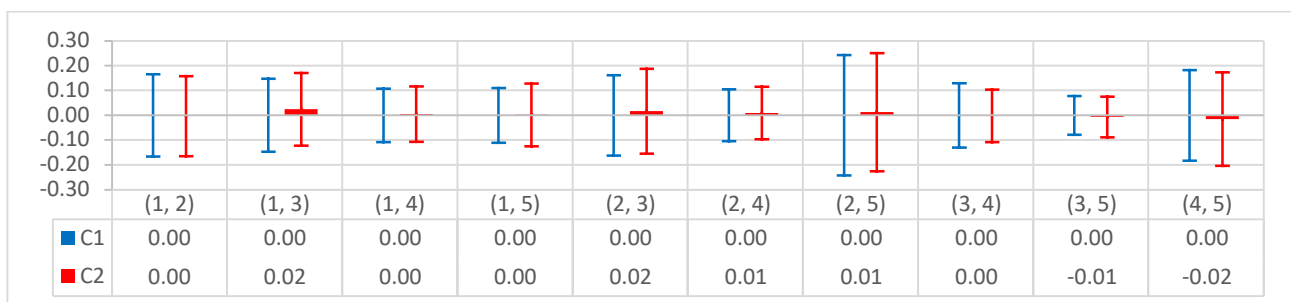


Figure 5. Difference between the baselines computed in calibration 1 (C1) and in calibration 2 (C2) ± MAD. The comparison is based on the values obtained from the filtered dataset. Values expressed in millimetres.

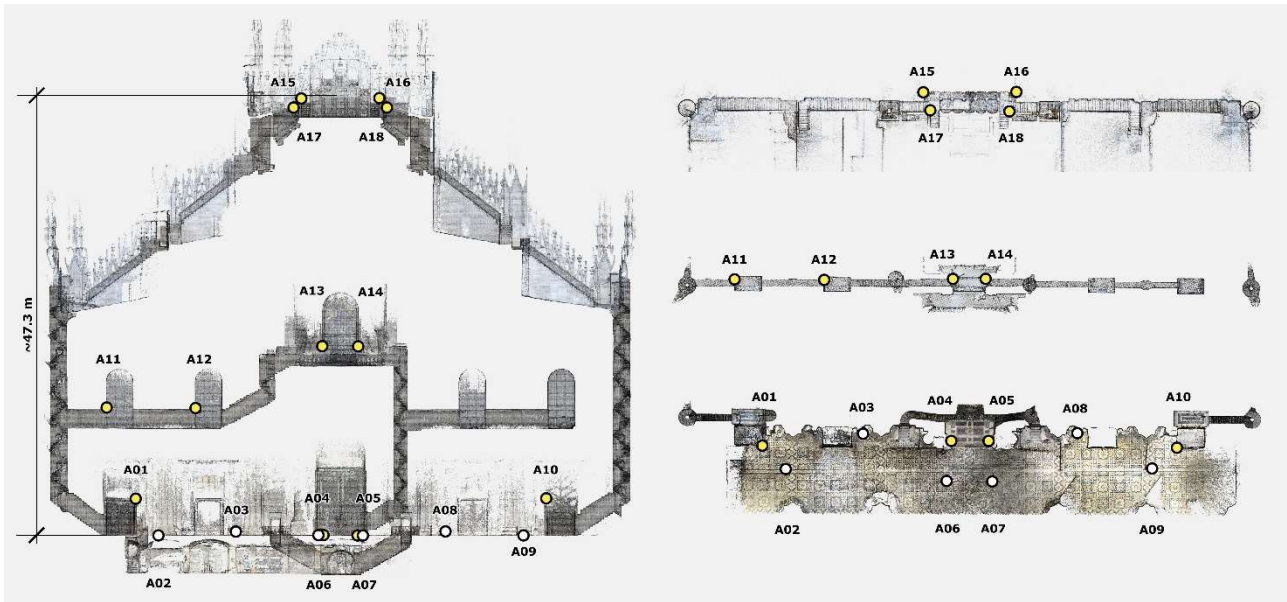


Figure 6. Point cloud result of Path A. Elevation view (left) and top view at three levels (right). According to Table 2, points in white are used as GCPs in the “max drift check”.

A check on the stability of the multicamera system was also performed by repeating the baseline computation twice: once before performing acquisitions for the test, and a second one at the end of the tests. The results obtained are described below. To perform the calibration, a small room, available on site, was set up for the task (Figure 4). The room measures approximately L:2m; W:1m; H:2, it has a good texture to be used for the Structure from Motion (SfM) and was also set up with photogrammetric markers whose coordinates were accurately derived. Using the calibration room, two image datasets were acquired with the multicamera system by programming a timed acquisition at 1 frame per second and rotating the system in all directions. The two datasets were then processed to derive for each camera pair a sample of approximately 100 estimated distances.

The values of the baselines were then computed by taking the median of these samples as a robust estimator was needed in the presence of outliers. Table 1 shows the values obtained for each camera pair for both calibrations (C1 and C2) along with the Median Absolute Distance from the median (MAD) as an indicator of sample dispersion as Nocerino et. al. (2018). Optimized baselines values were finally calculated by computing the median of the filtered datasets (FD) of the samples, after removing outliers (Table 1). Outliers were identified using the modified Z-score (1) as presented by Iglewicz & Hoaglin (1993), a threshold of  $M_i \geq 3.0$  was chosen to identify and discard outliers.

$$M_i = \frac{0.6745(x_i - \tilde{x})}{MAD} \quad (1)$$

where  $\tilde{x}$  = median  
 MAD = median of the absolute distances from the median

Finally, a comparison was made between the two calibrations obtained ~2 hours apart, before and after the tests were carried out. The graph and the table in Figure 5 show the difference between the distances obtained from the two calibrations (C1 and C2) and the values calculated by C1. It is possible to see how the difference between the two calibrations are negligible: max 0.02mm, far below the uncertainty of the calibration.

## 5. RESULTS

The acquired dataset for each of the five paths (Figure 2) were processed using Agisoft Metashape to carry out the SfM and to perform the evaluations. The computed baselines were imposed as constraints during the image orientation together with a preliminary calibration of the interior orientation parameters. At the end of the process the reconstructions were checked for gross errors that would eventually be fixed manually by re-orienting incorrectly positioned images. For the most part the acquisitions did not require manual processing after SfM.

ID	Path A							
	global check				max drift check			
	Err.	x	y	z	Err.	x	y	z
A01	3.7	-1.4	2.2	-2.6	3.5	-0.8	3.1	1.5
A02	5.0	-2.4	1.9	-3.9	3.4	-2.4	2.4	0.4
A03	3.2	-0.9	1.1	-2.9	1.8	-0.9	1.4	0.6
A04	3.6	-0.6	-0.3	-3.5	0.8	-0.8	-0.2	-0.2
A05	3.8	-0.9	-0.5	-3.7	1.3	-1.2	-0.4	-0.5
A06	4.6	-1.6	-0.4	-4.3	1.9	-1.9	-0.2	-0.3
A07	5.2	0.3	-1.4	-5.0	1.8	0.0	-1.3	-1.2
A08	5.0	3.5	0.2	-3.5	3.3	3.2	0.1	-0.8
A09	3.8	2.6	-2.2	-1.6	3.5	2.0	-2.4	1.4
A10	4.0	3.0	-2.2	-1.5	3.8	3.0	-2.1	1.1
A11	2.2	-1.0	1.8	0.7	5.7	0.8	3.6	4.3
A12	1.0	0.4	0.7	0.6	5.0	2.2	2.3	3.9
A13	5.4	-3.4	-2.0	3.7	6.5	-1.0	0.0	6.4
A14	5.6	-2.6	-3.0	4.0	6.7	-0.2	-1.1	6.7
A15	6.1	0.3	0.6	6.0	11.7	5.9	5.1	8.8
A16	6.7	3.2	1.7	5.7	13.3	8.7	6.0	8.1
A17	5.7	0.6	1.0	5.6	12.0	6.4	5.5	8.6
A18	6.0	1.3	0.3	5.8	12.0	6.9	4.7	8.5
max	6.7	3.2	1.7	5.7	13.3	8.7	6.0	8.1

Table 2. Error check of Path A. For “global check” all points are used as CPs, while for “max drift check” points highlighted in grey (white in Figure 6) are used as GCPs in a similarity transformation. All errors are expressed in centimetres.

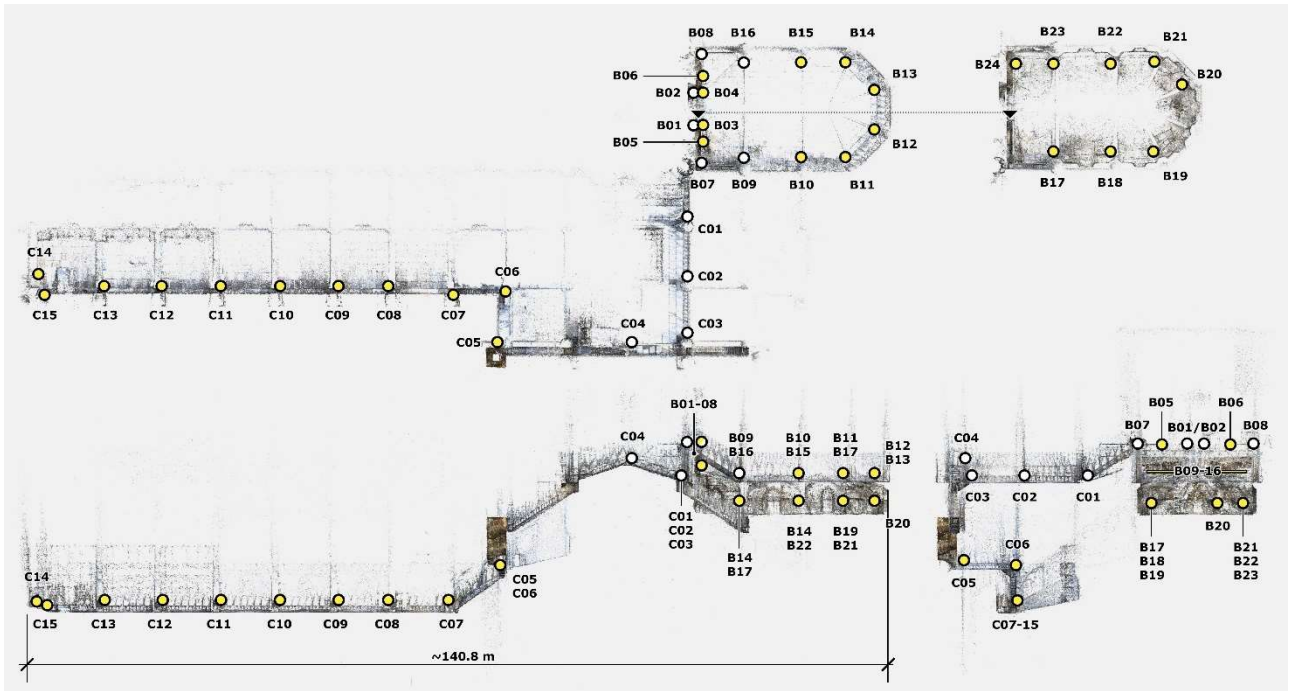


Figure 7. Point cloud result of Path B and Path C. Top views (top) and elevation views (bottom): front elevation bottom left and side elevation bottom right. According to Table 3 “Path B” and “Path C”, points in white are used as GCPs in the “max drift check”.

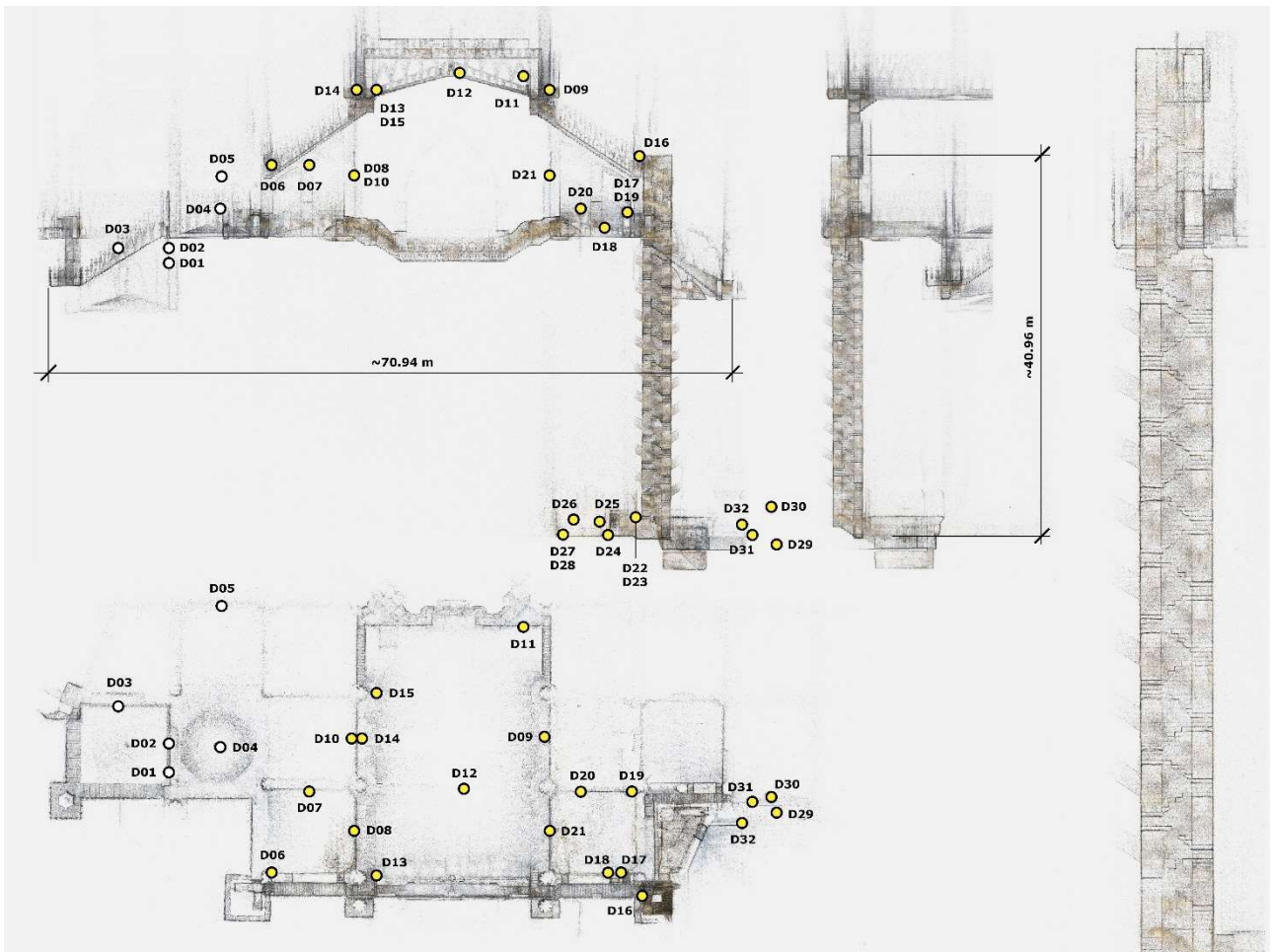


Figure 8. Point cloud result of Path D. Elevation views (top) and top views (bottom). On the right side a zoom of the spiral staircase. According to Table 3 “Path D”, points in white are used as GCPs in the “max drift check”.

At this point a set of CPs were identified along the paths. Reference coordinates were obtained from existing point clouds with an accuracy of ~2cm. Table 2 and Table 3 in this section reports the resulting error (centimetres) for all paths of the two evaluations described in Section 3. In Table 2 we can see the results of Path A, the only closed loop acquisition that resulted in a maximum error on 6.7cm for the "global check" and a

maximum error of 13.3cm for the "max drift check". At points A11-A12 there is already an accumulated error of ~5cm and after that the error increases the most, where the path continues in the outdoor environment of the rooftop.

Path B								
ID	global check				max drift check			
	err.	X	Y	Z	err.	X	Y	Z
B01	2.6	0.9	2.3	0.9	1.6	0.1	1.6	-0.5
B02	5.5	2.6	0.3	4.8	3.8	1.9	-0.3	3.3
B03	1.9	1.5	1.2	0.2	1.3	0.5	0.3	-1.1
B04	2.1	0.8	1.9	0.6	1.2	0.0	1.1	-0.6
B05	1.8	1.4	1.1	-0.1	1.6	0.6	0.3	-1.4
B06	2.1	0.8	1.9	0.3	1.7	0.2	1.4	-0.9
B07	1.2	-0.1	1.1	0.4	1.5	-1.2	0.0	-1.0
B08	1.1	0.9	-0.6	0.1	1.6	0.2	-1.2	-1.0
B09	1.5	-0.2	1.3	0.7	1.1	-1.1	0.0	-0.2
B10	0.6	-0.3	0.3	0.4	1.6	-0.9	-1.3	0.3
B11	1.4	-1.0	0.7	0.7	2.1	-1.4	-1.1	1.2
B12	1.0	-0.6	-0.5	0.6	2.9	-0.7	-2.3	1.5
B13	1.5	-0.5	-0.8	1.2	3.2	-0.5	-2.4	2.1
B14	0.7	-0.1	-0.1	0.7	1.9	-0.1	-1.4	1.3
B15	1.0	-0.8	0.2	0.5	1.5	-1.0	-1.0	0.6
B16	1.0	0.5	0.8	0.0	0.7	0.0	0.0	-0.7
B17	1.1	-0.8	0.6	-0.4	2.5	-1.9	-1.0	-1.3
B18	2.6	-1.8	-0.9	-1.8	4.2	-2.6	-2.7	-1.9
B19	5.0	-3.7	-2.1	-2.5	6.4	-4.3	-4.2	-2.0
B20	3.7	-0.5	-3.4	-1.2	5.3	-0.7	-5.3	-0.3
B21	4.7	-1.7	-4.0	-1.8	6.0	-1.9	-5.6	-1.2
B22	2.7	-0.5	-2.4	-1.0	4.0	-0.9	-3.8	-0.9
B23	1.3	0.6	-0.5	-1.0	2.4	-0.1	-1.7	-1.7
B24	3.9	2.8	1.8	-2.0	3.9	2.0	0.8	-3.2
max	5.5	2.6	0.3	4.8	6.4	-4.3	-4.2	-2.0

Path C								
ID	global check				max drift check			
	err.	X	Y	Z	err.	X	Y	Z
C01	10.3	-3.5	-8.5	4.6	2.4	1.4	-1.9	0.1
C02	8.8	-3.2	-7.3	3.7	1.9	1.1	-1.4	-0.5
C03	7.5	-5.3	-3.4	4.1	2.4	-1.5	1.8	0.3
C04	6.8	-4.2	-4.1	3.5	1.8	-1.0	1.5	0.1
C05	5.9	-3.7	-0.7	-4.5	10.1	-2.0	6.9	-7.1
C06	2.9	-0.6	-1.9	-2.2	8.3	1.5	6.4	-5.1
C07	4.3	-3.2	-0.5	-2.9	10.3	-1.6	8.5	-5.5
C08	2.4	-0.2	-1.0	-2.2	9.7	0.7	8.6	-4.4
C09	4.0	1.5	2.3	-2.8	13.5	1.8	12.5	-4.7
C10	3.8	2.4	2.8	-1.1	13.9	2.1	13.5	-2.6
C11	3.7	0.9	3.4	-1.3	14.8	-0.1	14.6	-2.5
C12	5.3	3.0	4.4	0.2	16.2	1.4	16.1	-0.7
C13	5.8	2.8	4.8	1.4	17.3	0.6	17.2	1.0
C14	7.1	6.2	3.5	-0.3	16.9	3.5	16.5	-0.4
C15	9.6	7.2	6.3	-0.5	19.6	4.3	19.1	-0.6
max	10.3	-3.5	-8.5	4.6	19.6	4.3	19.1	-0.6

Path D								
ID	global check				max drift check			
	err.	X	Y	Z	err.	X	Y	Z
<b>D01</b>	8.3	-3.8	3.9	-6.3	1.1	-0.1	-0.8	-0.8
D02	8.1	-3.1	4.8	-5.7	0.6	0.6	0.0	-0.1
<b>D03</b>	9.6	-4.2	3.4	-7.9	1.7	-0.4	-1.5	-0.6
D04	5.9	-2.9	3.4	-3.9	1.6	1.5	-0.5	0.3
D05	12.9	-9.4	8.6	-2.2	3.5	-1.6	2.9	1.2
D06	2.9	-1.2	-2.5	-0.9	6.7	4.7	-4.7	1.2
D07	2.1	-1.9	0.7	-0.4	3.9	3.2	-1.9	1.1
D08	2.7	-1.7	1.7	-1.4	3.6	3.2	-0.8	-1.4
<b>D09</b>	7.5	4.0	0.7	6.3	9.8	9.7	0.2	1.1
<b>D10</b>	6.2	-0.8	6.2	-0.1	5.1	3.8	3.4	0.3
D11	8.0	1.3	3.7	6.9	8.1	7.0	2.7	3.2
D12	3.9	1.9	-1.2	3.2	8.6	8.4	-1.6	0.4
D13	3.5	-0.1	-2.3	2.7	7.5	6.7	-3.0	1.8
D14	3.2	-0.8	0.5	3.0	6.6	5.6	-0.7	3.4
<b>D15</b>	4.0	-0.6	1.0	3.8	6.8	5.6	-0.4	3.8
D16	8.8	7.1	-1.6	5.0	12.1	11.4	-2.4	-3.5
<b>D17</b>	7.5	7.0	-2.0	1.7	12.5	10.1	-4.0	-6.1
D18	6.8	6.5	-1.8	1.4	11.8	9.3	-4.1	-6.0
<b>D19</b>	6.7	5.4	0.9	3.8	9.1	8.2	-1.4	-3.8
D20	5.0	4.4	-0.2	2.3	8.8	7.5	-2.6	-3.9
D21	5.5	4.0	-3.0	2.2	9.9	8.0	-4.8	-3.3
<b>D22</b>	2.7	2.5	-0.9	0.5	11.5	-1.5	-8.6	-7.4
D23	3.8	-0.9	-3.7	0.7	14.3	-4.9	-11.4	-7.2
D24	6.4	6.3	0.1	-0.9	11.6	2.3	-7.7	-8.3
D25	5.7	5.5	-1.5	-0.5	12.1	1.7	-9.2	-7.7
D26	9.6	9.0	-3.1	0.4	13.6	5.5	-10.8	-6.0
<b>D27</b>	10.0	7.2	-6.8	-1.6	17.0	3.3	-14.9	-7.5
D28	13.2	1.6	-12.9	-2.2	22.8	-2.6	-21.4	-7.6
D29	11.6	-8.6	7.8	-0.4	18.4	-13.9	0.0	-12.1
D30	12.5	-10.1	7.3	-1.0	19.4	-14.7	0.0	-12.6
<b>D31</b>	11.2	-8.7	7.0	-1.2	18.4	-13.6	-0.6	-12.4
D32	8.6	-5.4	6.7	-0.6	15.2	-9.9	-0.7	-11.5
Max	13.2	1.6	-12.9	-2.2	22.8	-2.6	-21.4	-7.6

Path E								
ID	global check				max drift check			
	err.	X	Y	Z	err.	X	Y	Z
E01	4.3	2.6	3.5	-0.4	1.1	0.9	0.3	-0.5
E02	3.0	2.0	2.1	-0.5	1.3	0.2	-0.8	-0.9
E03	3.9	1.1	3.2	2.0	1.7	-1.0	0.4	1.4
E04	3.4	1.3	3.1	0.5	0.2	-0.1	0.2	0.1
E05	2.9	0.8	2.5	1.2	1.1	-1.1	0.1	0.0
E06	3.5	-0.5	-3.2	-1.5	6.6	-2.6	-5.2	-3.1
E07	4.3	-1.8	-4.0	0.1	8.0	-5.2	-5.8	-1.7
E08	3.9	-2.4	-2.4	-1.8	8.4	-6.3	-4.1	-3.9
E09	5.8	-3.0	-4.9	0.4	9.3	-6.5	-6.4	-1.9
max	5.8	-3.0	-4.9	0.4	9.3	-6.5	-6.4	-1.9

Table 3. Error check of Path B, C, D and E. For "global check" all points are used as CPs, while for "max drift check" points highlighted in grey are used as GCPs in a similarity transformation. Only for Path D an additional check was performed by using GCPs in the bundle adjustment (Bold IDs), the results are described in the conclusions. All errors are expressed in centimetres.

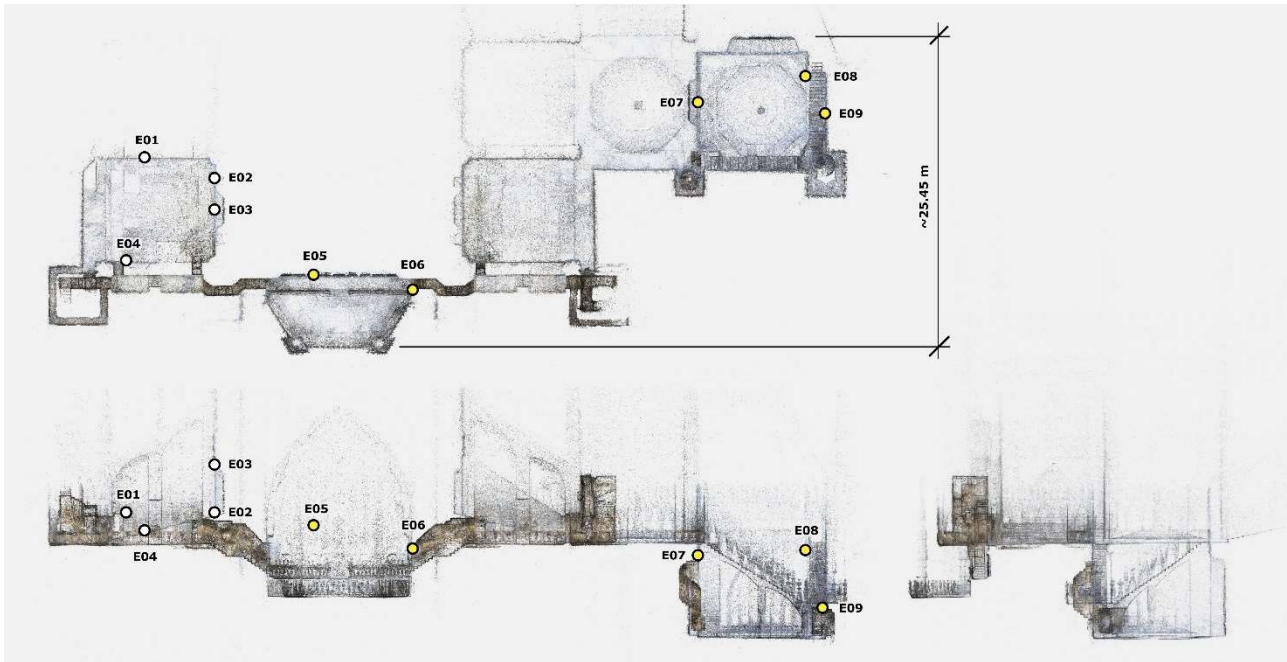


Figure 9. Point cloud result of Path E. Top view (top) and elevation views (bottom): front elevation bottom left and side elevation bottom right. According to Table 3 “Path E”, points in white are used as GCPs in the “max drift check”.

	N° Images	N° Sequences	Acq. duration	Path length	Max error	Drift error (100m)
Path A	13700	5	70 min	~290 m	13.3 cm	4.6 cm
Path B	1630	4	35 min	~295 m	6.4 cm	2.2 cm
Path C	4460	1	15 min	~245 m	19.6 cm	8.0 cm
Path D	12015	8	120 min	~465 m	22.8 cm	4.9 cm
Path E	6100	4	45 min	~256 m	9.3 cm	3.6 cm

Table 4. Main Data of the five path acquisitions. Path length is computed as the distance travelled by the multicamera in the outward acquisition direction only.

Despite the error, at a visual inspection, no distortions are detectable in the Reconstruction. Showing that the multicamera system can maintain the overall shape of the environment and orthogonality of the different elements. This is confirmed also by the results of “Path C” that is instead an open loop acquisition carried out in only the outward direction. In the “max drift check” it can be noticed that immediately after control point C04, at C05 there is an accumulated error of ~10cm, mostly concentrated in the Z direction, suggesting a distortion in the reconstruction of the enclosed spiral staircase connecting the two levels of the roofs. After that, the error increases of around 9cm in the remaining ~80m of passage.

A similar drift error can be observed in the results of “Path E” where a total error of around 9cm accumulates in a path length of around 256m (Table 4).

A better result is obtained from “Path B” where the “max drift check” resulted in a max error of 6.4cm that would be just suitable for 1:100 representation scale even without any constraints. Results are also positive for “Path D” where the entire open-ended path, that is the most complex of the set, resulted in a “max drift check” error of 22cm that considering the length of the instrument trajectory produced a contained drift deviation (Table 4). Moreover, for “Path D”, the visual inspection of the spiral staircase, the narrow connection between the roof level and the grounds, shown no noticeable distortions or bends in the reconstruction. This is confirmed by the errors that did not increase significantly from the top to the bottom of the staircase. Table 4 summarize the main data of the five acquisitions and helps to draw some conclusion on the behaviour of the

multicamera system. The “path length” is the distance travelled by the multicamera system in the outward direction. The “drift error” is computed from the max error obtained in the “max drift check” for each path divided then by the path length, results are normalized on a 100m metres run. The multicamera system average performance can be described best by Path A, Path D and Path E with an average drift error in the order of ~4.5cm every 100m of a two-ways trajectory. The drift error is double for Path C, where the entire acquisition consists of the outward acquisition, with no return path ever acquired. The drift error is instead half the average for Path B, for this test the acquisition was slower since the vaults rooms acquired are larger than the average passage and the acquisition focused more to acquire all the geometry.

## 6. CONCLUSIONS

The results of the test show the potential of the proposed approach. The multicamera system was always able to reconstruct the whole paths in all their parts and in short time (Table 4). No distortion or bends in the reconstructed trajectory are visible. In the worst-case scenario of unconstrained open loop paths, the overall shape and orthogonality of elements are still preserved. Looking at the staircase zoom in Figure 8 and at the mesh model view of Figure 10 it is possible to conclude that the proposed system can be used effectively to generate 3D models and to trace 2D drawings up to scale 1:50, at least locally.

Moreover, it can complement other survey techniques to measure complex areas.

On the other hand, the results also prove that, at the current development of the multicamera system, GCPs are needed to constraint, control and improve the results within an architectonic accuracy also globally. For instance, for "Path D", the longest acquired: if some GCPs distributed all along the survey trajectory are used (see Table 3 "Path D", target ID in bold), the root mean square error of the CPs lowers to 3.9cm and that of the GCPs is 3.6cm (the reference points accuracy is ~2cm).

For an actual proper 3D survey, the proposed solution yields results suitable for the scale 1:100 up to 1:50. And even in the complete absence of constraints the reconstructions are complete and free from obvious bends and distortions; in this scenario we can expect a drift of about 4.5cm every 100m measured both ways.

Nevertheless, the unconstrained max drift error should be improved. The main issues encountered during the tests were the following: (i) uneven lighting, the camera's dynamic range is not ideal for all conditions, image processing can be tested to reduce the contrast in the scenes; (ii) relative orientation, for now only the baselines were exploited to constrain the multicamera, rotation can be implemented as well; (iii) length of the processing time, the processing time can be shortened by implementing a real-time pre processing of the data during the acquisition.

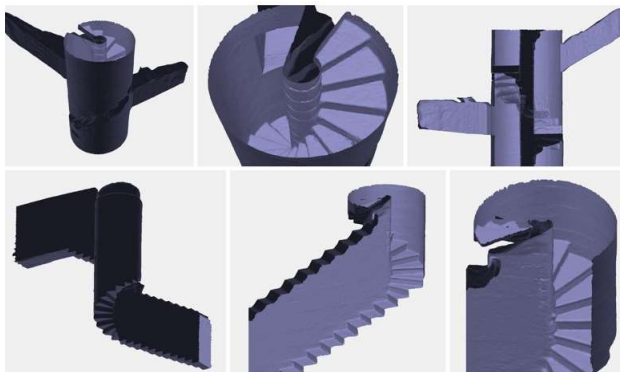


Figure 10. 3D view of portion of the mesh model produced from the acquisition of Path A (top).

## 7. FUTURE WORKS

Future developments of the multicamera system can concentrate on two main aspects, the first is the improvement of the usability and the effectiveness of the current solution: this includes the implementation of the full multicamera constraints and the implementation of image processing strategy to improve the lighting of the scene which is also critical for the texturing of the model and the coloring of the point cloud. The second aspect is the development of new features that could expand the capabilities of the device: first, there is the implementation of real-time processing and secondly there is the integration of additional positioning and mapping sensors along with the photogrammetric multicamera.

## ACKNOWLEDGEMENTS

The authors would like to thank Veneranda Fabbrica del Duomo di Milano, especially the director Eng. Francesco Canali for supporting this work by making all tests possible and Elizaveta Gradusova for the work carried out for her master thesis.

## REFERENCES

- Barazzetti, L., Previtali, M., and Roncoroni, F., 2017. 3D modelling with the Samsung gear 360. *Int. Arch. Photogramm. Remote Sens. Spatial Inf. Sci.*, Vol. XLII-2/W3, pp. 85–90.
- Barazzetti, L., Previtali, M., & Scaioni, M., 2020. Procedures for condition mapping using 360° images. *ISPRS International Journal of Geo-Information*, Vol. 9(1), pp. 34.
- Iglewicz, B., & Hoaglin, D., 1993. Volume 16: How to Detect and Handle Outliers. *American Society for Quality Control, Milwaukee, WI. Quality Press.*
- Koehl, M., Delacourt, T., and Boutry, C., 2016. Image capture with synchronized multiple-cameras for extraction of accurate geometries. *Int. Arch. Photogramm. Remote Sens. Spatial Inf. Sci.*, Vol. XLIB1, pp. 653–660.
- Meyer, D. E., Lo, E., Klingspon, J., Netchaev, A., Ellison, C., and Kuester, F., 2020. TunnelCAM- a HDR spherical camera array for structural integrity assessments of dam interiors. *Electronic Imaging*, Vol. 2020(7), pp. 227–1.
- Nocerino, E., Nawaf, M. M., Saccone, M., Ellefi, M. B., Pasquet, J., Royer, J.-P., and Drap, P., 2018. Multi-camera system calibration of a low-cost remotely operated vehicle for underwater cave exploration. *Int. Arch. Photogramm. Remote Sens. Spatial Inf. Sci.*, Vol. XLII-1, pp. 329–337.
- Nocerino, E., Menna, F., Farella, E., and Remondino, F., 2019. 3D Virtualization of an underground semi-submerged cave system. *Int. Arch. Photogramm. Remote Sens. Spatial Inf. Sci.*, Vol. XLII-2/W15, pp. 857–864.
- Panella, F., Roecklinger, N., Vojnovic, L., Loo, Y., and Boehm, J., 2020. Cost-benefit analysis of rail tunnel inspection for photogrammetry and laser scanning. *Int. Arch. Photogramm. Remote Sens. Spatial Inf. Sci.*, Vol. XLIII-B2-2020, pp. 1137–1144.
- Perfetti, L., Polari, C., & Fassi, F., 2017. Fisheye photogrammetry: tests and methodologies for the survey of narrow spaces. *Int. Arch. Photogramm. Remote Sens. Spatial Inf. Sci.*, Vol. XLII-2/W3, pp. 573–580.
- Perfetti, L., Polari, C., & Fassi, F., 2018. Fisheye Multi-Camera System Calibration for Surveying Narrow and Complex Architectures. *Int. Arch. Photogramm. Remote Sens. Spatial Inf. Sci.*, Vol. XLII-2, pp. 877–883.
- Perfetti, L., 2020. Multi-Camera Rig For 3D Reconstruction: Concept, Design and Accuracy Evaluation. in: *Luhmann, T., Schumacher, C., Photogrammetrie - Laserscanning – Optische 3D-Messtechnik, Beiträge der Oldenburger 3D-Tage 2020*, pp. 124–131.
- Shortis, M., Harvey, E., and Abdo, D., 2009. A review of underwater stereo-image measurement for marine biology and ecology applications. *Oceanography and Marine Biology*, pp. 257–292.
- Teo, T., 2015. Video-based point cloud generation using multiple action cameras. *Int. Arch. Photogramm. Remote Sens. Spatial Inf. Sci.*, Vol. XL-4/W5, pp. 55–60.